RSC Advances

PAPER

View Article Online
View Journal | View Issue

Cite this: *RSC Adv.*, 2024, **14**, 10089

Synergistic cobalt oxide/reduced graphene oxide/biochar nano-composite catalyst: harnessing the power of the catalyst for sustainable remediation of organic dyes and chromium(VI)

Amrita Priyadarsini, *[a] Chirasmayee Mohanty,[b] Spandan Nanda,[a] Abinash Mishra,[c] Nigamananda Das,[b] Nandita Swain,[a] Manasi Dash[c] and Pradip Kumar Jena*[a]

The exponential growth of industrial activities has led to a significant rise in the release of organic effluents, containing hazardous heavy metals and dyes, into the environment. These pollutants exhibit resistance to conventional biodegradation processes and are associated with carcinogenic properties, posing a severe threat to living organisms. In this context, the present research endeavours to address this environmental challenge through the development of an affordable and efficient photocatalyst, the Co_3O_4/reduced graphene oxide/biochar (CBG-10) heterostructure. The structural analysis of CBG-10, conducted through various techniques such as XRD, XPS, SEM, and optical property measurements, demonstrates its potential as a highly effective and easily recoverable catalyst for the mineralization of persistent pollutants like methylene blue, malachite green, and hexavalent Cr(VI). The recyclability of CBG-10 was confirmed through XRD studies, highlighting its stability and practical usability in wastewater purification. The photocatalytic behaviour of the catalyst was attributed to the generation of hydroxyl (•OH) and superoxide radicals ($•O_2^-$) during visible light illumination, as revealed by quenching experiments. The cost-effectiveness and stability of CBG-10 position it as a promising solution for addressing the challenges associated with the removal of stubborn organic contaminants from wastewater, thereby contributing to environmental protection and public health.

Received 9th February 2024
Accepted 20th March 2024

DOI: 10.1039/d4ra01031k

rsc.li/rsc-advances

1. Introduction

In recent decades, the escalating global population and rapid industrial expansion have led to profound challenges in maintaining the quality of water resources essential for human consumption and ecosystem health. The discharge of untreated industrial effluents, containing a plethora of contaminants such as synthetic dyes and heavy metals, has exacerbated the degradation of freshwater bodies, intensifying the scarcity of potable water in numerous regions worldwide.[1,2] Among these pollutants, chromium(VI) (Cr(VI)) stands out due to its prevalence alongside organic dyes in industrial processes, contributing to its classification as a priority pollutant by regulatory agencies like the United States Environmental Protection Agency (USEPA).[3–6] The complex aromatic structures of synthetic dyes render them highly stable and resistant to biodegradation, posing significant threats to aquatic ecosystems and human health due to their carcinogenic and mutagenic properties. Therefore, addressing the remediation of industrial effluents containing dyes and heavy metals is imperative to mitigate their adverse impacts on water quality and public health.

A diverse array of remediation methods encompassing physical, chemical, and biological approaches have been developed to tackle the challenges posed by organic dyes and Cr(VI) contamination in wastewater.[7–12] Among these, adsorption and photocatalytic degradation/reduction methods have garnered substantial attention for their efficacy, operational simplicity, and eco-friendly nature. While conventional carbonaceous adsorbents have been widely employed, recent years have witnessed significant exploration into nano- and hybrid adsorbents to enhance adsorptive removal efficiency. Furthermore, photocatalytic degradation, particularly the reduction of Cr(VI) to less toxic Cr(III) species and complete mineralization of dyes, holds promise as a sustainable and environmentally friendly approach.[13–18] The development of semiconductor photocatalysts, including oxides, sulphides, and nitrides, has emerged as a focal point in this domain, with efforts focused on

[a]*Department of Chemistry, College of Basic Science and Humanities, Odisha University of Agriculture and Technology, Odisha, India. E-mail: priyadarsiniamrita@gmail.com*
[b]*Department of Chemistry, Utkal University, Bhubaneswar 751004, Odisha, India*
[c]*Department of Genetics and Plant Breeding, College of Agriculture, Odisha University of Agriculture and Technology, Odisha, India*

enhancing photocatalytic efficiency under various light sources through material design and engineering.

In this context, the present study aims to investigate the potential of Co_3O_4-based materials as robust photocatalysts for the remediation of organic dyes and Cr(VI) contamination in wastewater.[19] Leveraging facile synthesis methods and inherent chemical stability, Co_3O_4 materials offer a versatile platform for photocatalytic applications, underscored by their distinctive semiconductor properties and tunable bandgaps. Notably, the integration of Co_3O_4 with graphene oxide, renowned for its remarkable properties, presents an avenue for enhancing photocatalytic performance across diverse applications.

The development of Co_3O_4/reduced graphene oxide/biochar composite photocatalysts represents a significant advancement, offering a multifunctional approach towards environmental remediation by harnessing the unique properties of each component for enhanced efficiency in pollutant degradation and catalyst recovery.[20] The demonstrated photocatalytic ability of the combination of Co_3O_4, reduced graphene oxide, and biochar, especially in the breakdown of difficult contaminants including chromium(VI), malachite green, and methylene blue. In the current work, a number of recyclable hybrid composites (CBG-*X*) containing reduced graphene oxide, biochar, and Co_3O_4 were synthesised, described, and their potential for the adsorptive and photocatalytic removal of dyes and Cr(VI) was evaluated. To the best of our knowledge, this is the first-ever report on the use of Co_3O_4/reduced graphene oxide/biochar composite an inexpensive, easily separable, highly reactive visible light active photocatalyst.

2. Experimental section

2.1 Materials

The main raw material used in this research was banana pseudo stem (BP), which was collected from banana plants near Bhubaneswar, Odisha. The present study used a variety of chemicals, such as graphite, methylene blue (MB), malachite green (MG) dye, potassium permanganate ($KMnO_4$) were from (Merck/S.D. Fine Chemicals), with high purity (≥99.0% assay). Hydrogen peroxide (H_2O_2), ethanol (C_2H_5OH), potassium dichromate ($K_2Cr_2O_7$), sodium carbonate (Na_2CO_3) were from SRL with high purity, sodium nitrate ($NaNO_3$), graphite, and hydrogen peroxide (H_2O_2) were from Sigma Aldrich with high purity (≥99.0% assay). All aqueous solutions used in the synthesis process were carefully produced using double distilled water.

2.2 Preparation of biochar

In the synthesis process of banana pseudo stem biomass, meticulous steps were undertaken to prepare the material for further analysis and application. Initial cleansing with tap water followed by distilled water ensured the removal of surface contaminants, maintaining the integrity of the biomass. Subsequently, the biomass was meticulously sectioned into smaller pieces, optimizing its surface area for subsequent treatments. Drying in an oven at 100 °C until reaching a consistent weight effectively removed moisture content, a critical prerequisite for subsequent processing steps. Finely powdering the dried biomass using a pulveriser equipped with a 250 mm sieve further homogenized the material, enhancing its reactivity. Pyrolysis, the crucial step in the synthesis process, was conducted in a muffle furnace under a continuous flow of nitrogen gas at 500 °C for 1 hour, employing a heating rate of 10 °C min^{-1}. This controlled thermal decomposition process is pivotal in transforming the biomass into valuable products, thus establishing a foundation for exploring its potential applications in various fields.

2.3 Synthesis of graphene oxide

In a meticulously conducted procedure, graphene oxide (GO) was synthesized through a series of precisely controlled steps. The process commenced with the addition of 46 mL of concentrated sulfuric acid to a mixture containing 1 g of concentrated graphite powder and 1 g of $NaNO_3$, all within an ice bath, setting the foundation for subsequent reactions. Following a 15-minute stirring period, 8 g of potassium permanganate was gradually introduced into the mixture, ensuring thorough incorporation through continued stirring at room temperature for two hours. The addition of 80 mL of distilled water to the mixture facilitated further reactions, with an additional hour of stirring enhancing homogeneity. A subsequent introduction of 200 mL of distilled water, followed by the careful addition of H_2O_2 until gas evolution ceased, marked the final steps of the synthesis process. The resultant GO was meticulously separated *via* centrifugation, followed by a drying step at 70 °C, ensuring the preservation of its structural integrity and chemical properties for future utilization. This methodical synthesis approach lays the groundwork for the production of high-quality graphene oxide, offering promising prospects for diverse applications across various scientific disciplines.

2.4 Synthesis of CO_3O_4

In the present study, the synthesis of Co_3O_4 nanoparticles was successfully achieved through a Co-precipitation process. Initially, 2.5 g of $CoCl_2 \cdot 6H_2O$ was dissolved in deionized water and magnetically stirred for 20 minutes. Subsequently, this solution was introduced into a 20 mL sodium carbonate solution (1 M) and stirred at a controlled temperature of 70.0 °C for a duration of 5 hours. The resultant light purple-coloured precipitates were collected *via* centrifugation at 10 000 rpm after 6 hours, and three washing cycles were performed using pure alcohol and deionized water.[21] The collected precipitates underwent a drying process for 12 hours at 80.0 °C in an oven, followed by calcination for three hours at 500.0 °C in an electric furnace. Morphological characteristics of the Co-precipitation technique product were analysed using specialized instrumentation.[22]

To compare the activity of the pristine cobalt oxide, a separate synthesis of cobalt oxide (Co_3O_4) was carried out at 350 °C. In this procedure, 3 g of $CoCl_2 \cdot 6H_2O$ and 1 M Na_2CO_3 were added to the mixture under constant stirring. After an

additional hour of stirring, a dense purple-coloured solution developed. The resulting combination underwent hydrothermal treatment for 5 hours at 120 °C in Teflon-lined autoclaves. The obtained slurry was meticulously washed with ethanol and water before being dried overnight in an oven at 80 °C. Subsequently, the dried sample was calcined for 5 hours at 350 °C, yielding a powdered form of the dark-coloured cobalt oxide (Co_3O_4). The Powder X-ray Diffraction (PXRD) analysis of the synthesized cobalt oxide exhibited excellent agreement with the standard reference pattern (JCPDS# 01-073-1701). The diffraction peaks at $2\theta = 19.00, 31.27, 36.84, 38.54, 44.81, 55.65, 59.36, 65.23, 68.63, 74.11$, and 77.34 were identified as (111), (220), (311), (222), (400), (422), (511), (440), (531), (620), and (533), respectively (Fig. 1(e)). These findings highlight the successful synthesis of Co_3O_4 nanoparticles through both Co-precipitation and hydrothermal methods, providing valuable insights into their structural characteristics for potential applications.

2.5 Synthesis of CO_3O_4/biochar/rGO(CBG-*X*)

A novel composite material termed CBG (Co_3O_4/biochar/graphene) was synthesized through a multi-step procedure. Initially, a predetermined quantity of reduced graphene oxide (rGO) and biochar were combined with distilled water and subjected to ultrasonication for one hour to ensure homogenous dispersion. Subsequently, cobalt chloride hexahydrate ($CoCl_2 \cdot 6H_2O$) and sodium carbonate (Na_2CO_3) were introduced into the mixture under stirring conditions, resulting in the formation of a dense purple-coloured solution. This solution underwent hydrothermal treatment at 120 °C for five hours in Teflon-lined autoclaves. The resulting slurry was thoroughly rinsed with ethanol and water to remove any residual impurities, followed by drying overnight at 80 °C. The dried sample was then subjected to calcination at 350 °C for five hours, leading to the formation of powdered CBG. Various weight percentages of biochar/rGO (2, 5, 10) were incorporated into the composite, with resulting materials designated as CBG-*X*, where '*X*' represents the percentage of biochar/rGO used in the synthesis (Scheme 1).

2.6 Characterization techniques

The synthesized composite materials underwent meticulous characterization employing an array of advanced analytical methods, including X-ray Diffraction (XRD), Diffuse Reflectance UV-Visible Spectroscopy (UV-Vis DRS), Fourier Transform Infrared Spectroscopy (FT-IR), Photoluminescence (PL) spectroscopy, X-ray Photoelectron Spectroscopy (XPS), and Scanning Electron Microscopy (SEM) equipped with Energy Dispersive X-ray (EDX). X-ray diffraction patterns were acquired in the 2θ range of 10–80°, utilizing a Phillips PW-1710/PW-1729 X-ray diffractometer with CuKα ($\lambda = 1.542$ Å) radiation. Morphological features were assessed through Scanning Electron Micrographs (SEM), employing a TESCAN VEGALSV instrument operating under an electrical field acceleration of 5 to 10 kV. Elemental analysis was performed using Energy Dispersive X-ray (EDX) spectroscopy in conjunction with SEM. X-ray Photoelectron Spectra (XPS) were acquired utilizing a UHV analysis system (SPECS, Germany) employing an AlKα monochromatic X-ray source ($E = 1486.6$ eV). UV-Visible Diffuse Reflectance Spectra (UV-Vis DRS) for diverse samples were recorded utilizing a Shimadzu (Model 2550) spectrophotometer over a wavelength range of 200–800 nm, using $BaSO_4$ as the reference material. Fourier Transform Infrared (FT-IR) spectra of biochar, Co_3O_4, and CBG-*X* in KBr pellets were captured *via* a Thermo-Nicolet (Nexus 870) FT-IR spectrometer.

2.7 Adsorption/photocatalytic activity of dyes/Cr(VI)

The adsorption capabilities and photocatalytic performance of various hybrid composites, including biochar, CBG-2, CBG-5, CBG-10, Co_3O_4, and rGO, were investigated in the absence of light. Employing a thermostat water bath shaker at a constant temperature, the samples were tested for their adsorption behaviour towards dyes by combining specified amounts with dye solutions in conical flasks. Following pH adjustment and agitation, the nanoparticles were extracted, and the supernatant's absorbance was measured to determine the amount of adsorbed dye. Similar methodologies were employed to assess the adsorption of Cr(VI), with optimal pH values determined for sorption. UV-visible spectra were recorded to facilitate comparisons, and multiple experiments were conducted for each sample to ensure reliability. The amount of adsorbed dye (mg g^{-1}) on the sample was calculated using the mass balance equation (eqn (1)), where C_e represents the final equilibrium concentration of the dye in the solution (mg L^{-1}), q_e is the

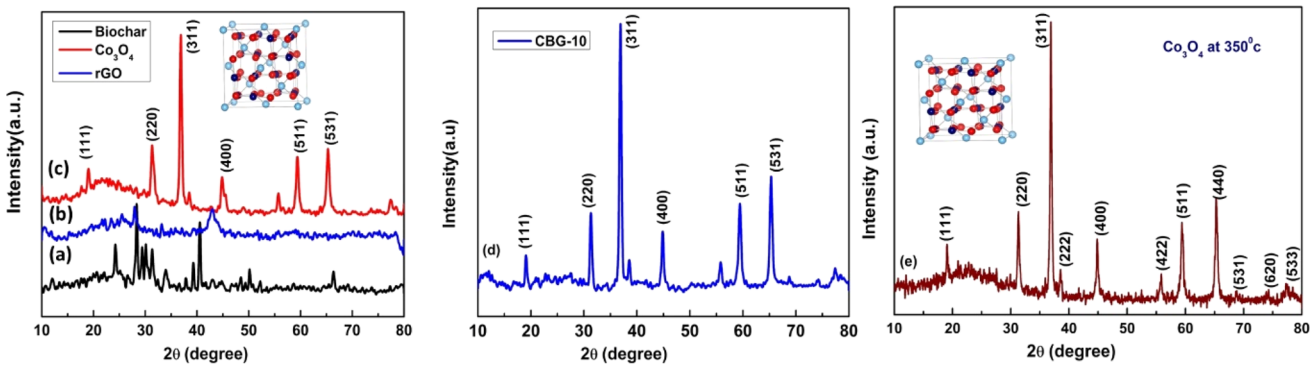

Fig. 1 XRD analysis of (a) biochar (b) rGO (c) Co_3O_4 at 500 °C (d) CBG-10 and (e) Co_3O_4 at 350 °C nanocomposite photocatalyst.

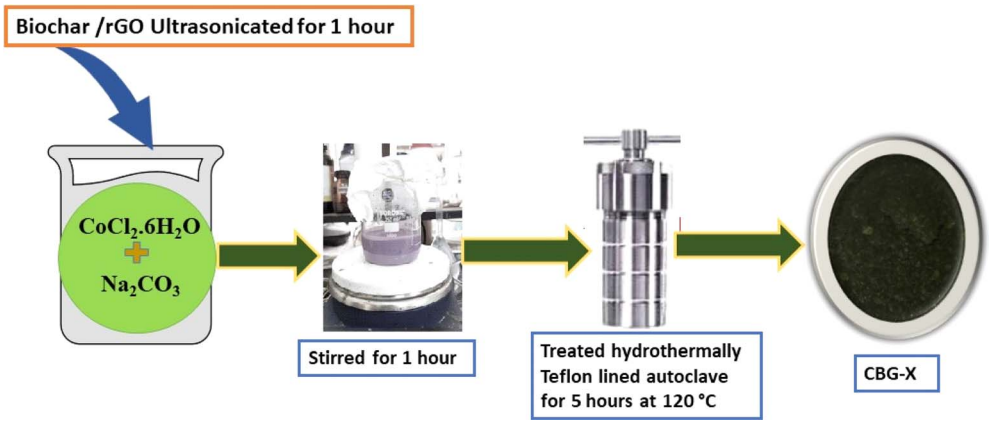

Scheme 1 Schematic representation of the synthesis of the CBG-*X* catalyst.

equilibrium adsorption capacity per gram of the adsorbent (mg g^{-1}), C_0 is the initial dye concentration in the solution (mg L^{-1}), V is the total solution volume (mL), and W is the weight of the adsorbent (g).

$$q_e = \frac{(C_0 - C_e)}{W} \times V \quad (1)$$

Furthermore, the photocatalytic efficacy of the tested materials was evaluated through the degradation of methylene blue (MB) and malachite green (MG) dyes. Batch photocatalytic experiments were conducted within a specialized reactor under visible light illumination, with continuous stirring to ensure homogeneous dispersion. Samples of 5 mL aliquots were withdrawn at regular intervals, and their absorbance was measured to calculate the degree of dye degradation. The integration of Co_3O_4 with biochar or rGO, particularly at a concentration of 10 wt%, demonstrated superior performance in both adsorption and photocatalytic analyses. The solution's temperature was maintained at 25.0 ± 0.5 °C by circulating water through the reactor's outer wall. The withdrawn samples were subjected to centrifugation, and the absorbance of the supernatant was determined at wavelengths of 620 nm for MG and 664 nm for MB. The degree of dye degradation was calculated using eqn (2), and all spectral measurements were conducted using an Agilent UV-visible spectrophotometer.

$$\text{Degradation } (\%) = \frac{(C_0 - C_t)}{C_0} \times 100 \quad (2)$$

In general, the comprehensive investigation of the adsorption behaviour and photocatalytic activity of various nanomaterials revealed promising results for the integration of Co_3O_4 with biochar or rGO, particularly at a 10 wt% concentration *i.e.* (CBG-10).

3. Results and discussion

In this study, X-ray diffraction (XRD) analysis was employed to investigate the structural properties of biochar Co_3O_4, reduced graphene oxide (rGO), and CBG-10 nanocomposites. The XRD patterns revealed distinct characteristics for each component. Pure reduced GO exhibited diffraction peaks at 24.4 and 43.2°, corresponding to the (002) and (111) crystal planes, respectively. The mineralogical composition of banana-waste biochar, as depicted in Fig. 1(a), demonstrated a broad hump with a centroid between 20 and 30°. Pristine Co_3O_4, shown in Fig. 1(c), exhibited diffraction peaks at 2θ values of 19.00, 31.2, 36.8, 44.8, 59.36, and 68.3 corresponding to the (111), (220), (311), (400), (511) and (531) crystal planes, in accordance with (JCPDS# 01-073-1701). The XRD pattern of the CBG-10 composite, illustrated in Fig. 1(d), displayed significant diffraction peaks for Co_3O_4, indicating the formation of the CBG-10 heterostructure without any additional phases or contaminants. Furthermore, Fig. 1(e) depicted the XRD diffraction pattern of Co_3O_4 at 350 °C, diffraction peaks at 2θ values of 19.00, 31.2, 36.8, 44.8, 59.36, 68.3, 74.1, and 77.3 corresponding to the (111), (220), (311), (400), (511), (531), (620), and (533) crystal planes, which closely matched the reference pattern (JCPDS# 01-073-1701).

In this study, the FTIR (Fourier Transform Infrared Spectroscopy) approach was utilized to analyse annealed cobalt oxide nanoparticles (Co_3O_4), biochar, and reduced graphene oxide (rGO). Fig. 2 illustrates the typical FTIR spectrum within the spectral region of 400–4000 cm^{-1} for the aforementioned materials. Analysis of the Co_3O_4 spectrum revealed distinct peaks at 572 cm^{-1} and 664 cm^{-1}, attributed to the Co–O shaking mode frequency and the bridging shake of the O–Co–O bond, respectively. Additionally, minor peaks observed at 1118 cm^{-1} were indicative of C–O stretching vibrations. The appearance of peaks at 2345 cm^{-1} suggested carbon absorption during the thermal interaction of metal oxides with the atmosphere, likely attributed to asymmetric vibration (C=O) of CO_2. Furthermore, the broad peak ranging from 3000 to 3400 cm^{-1} indicated the presence of C–N stretching of benzene rings, commonly associated with stretching vibrational modes from –NH groups and surface-adsorbed water molecules. Importantly, the intensity of FTIR peaks decreased as Co_3O_4 material was incorporated into biochar and reduced graphene oxide, suggesting an interaction between Co_3O_4 and biochar/rGO. These

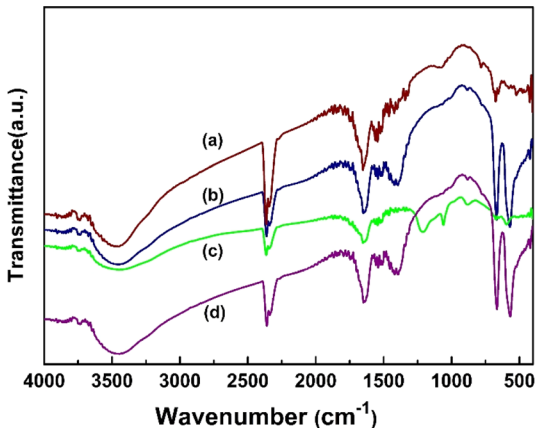

Fig. 2 FTIR survey of (a) biochar (b) CBG-10 (c) rGO and (d) Co_3O_4.

findings are consistent with XRD (X-ray Diffraction) data, highlighting the compatibility and potential applications of CBG-10 material in various fields.[22]

The morphological investigation conducted *via* scanning electron microscopy (SEM) unveiled a distinctive pleated laminar structure within the reduced graphene oxide/biochar (rGO/BC) composite, showcasing a heightened specific surface area. Fig. 3 illustrates the profound interplay between the components, particularly evident in the even dispersion of equally sized spherical Co_3O_4 particles across the rGO/BC sheets (Fig. 3(c)). This dispersion highlights the efficacy of the composite in providing numerous surface-active sites, indicative of enhanced specific surface area. Notably, the Co_3O_4 microspheres are intricately dispersed over the graphene oxide and biochar matrices, denoting successful Co_3O_4 loading onto the rGO/Biochar framework. The SEM micrograph (Fig. 3(c)) of the CBG-10 composite reveals the presence of numerous Co_3O_4 nanoparticles as discernible white dots, further corroborating successful loading onto the rGO/BC platform.[24] Additionally, the Energy Dispersive X-ray Spectroscopy (EDS) analysis (Fig. 3(d)) of CBG-10 provides elemental insights, while elemental mapping (Fig. 3(e)–(h)) further elucidates the distribution of carbon, oxygen, and cobalt within the composite, offering valuable insights into the structural integrity and potential applications of the synthesized material.[23]

The band energy gap (E_g) serves as a pivotal indicator in assessing the efficacy of a photocatalyst's light absorption capabilities. Through the utilization of Tauc plots and UV-Vis spectroscopy, as illustrated in Fig. 4, the bandgap values were discerned. Specifically, the determination of Eg *via* Tauc plots involved extrapolating the linear segment of the $(\alpha h\nu)^2$ curve against photon energy ($h\nu$). This analysis revealed a noteworthy enhancement in visible light absorption upon the incorporation of Co_3O_4 nanoparticles (NPs), leading to an observed reduction in the band gap of the composite CBG-10 from 2.0 eV, representative of pure cobalt oxide, to 1.5 eV. Such a reduction in band gap signifies an augmentation in the generation of photogenerated charge carriers, thereby indicating an improved photocatalytic performance of the composite material.

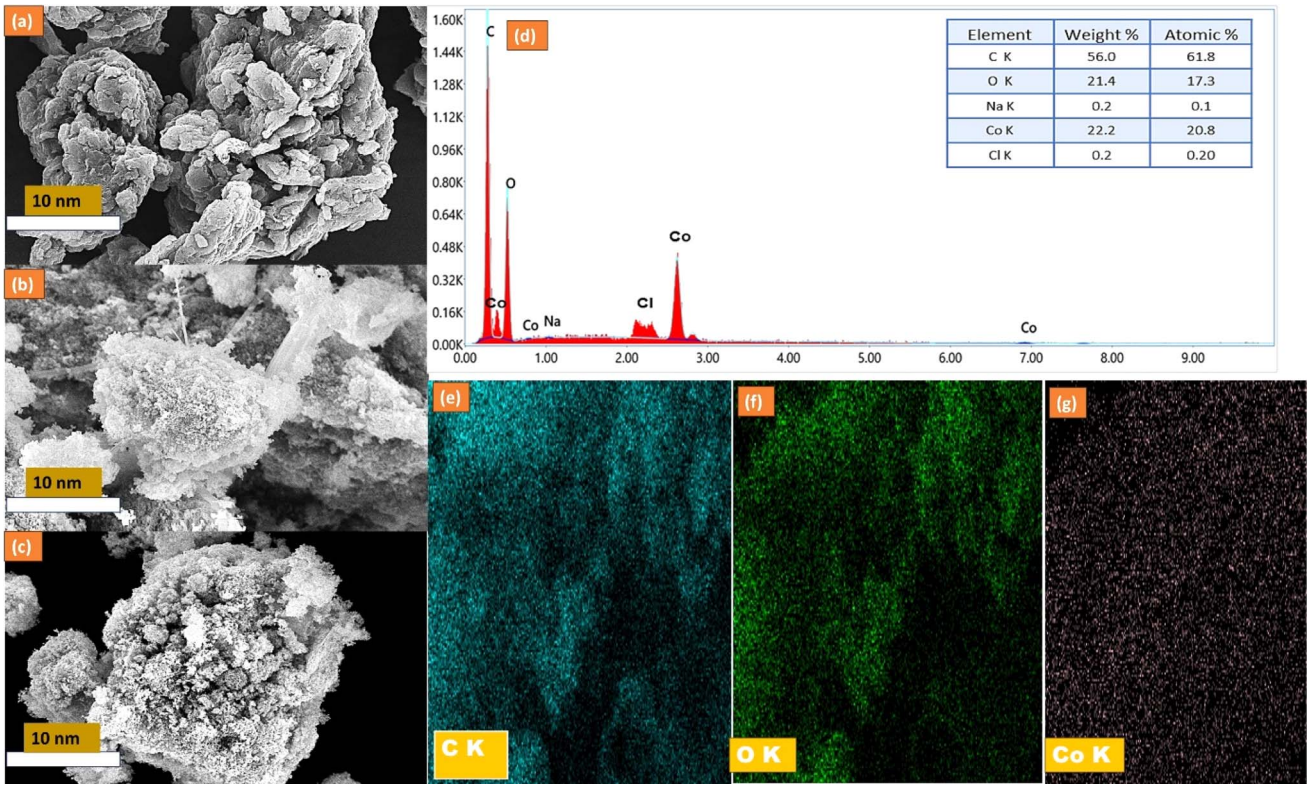

Fig. 3 SEM analysis of the rGO/biochar (a), Co_3O_4 (b), CBG-10 (c), EDS of CBG-10 (d), elemental mapping of C (e), O (f), and Co (g).

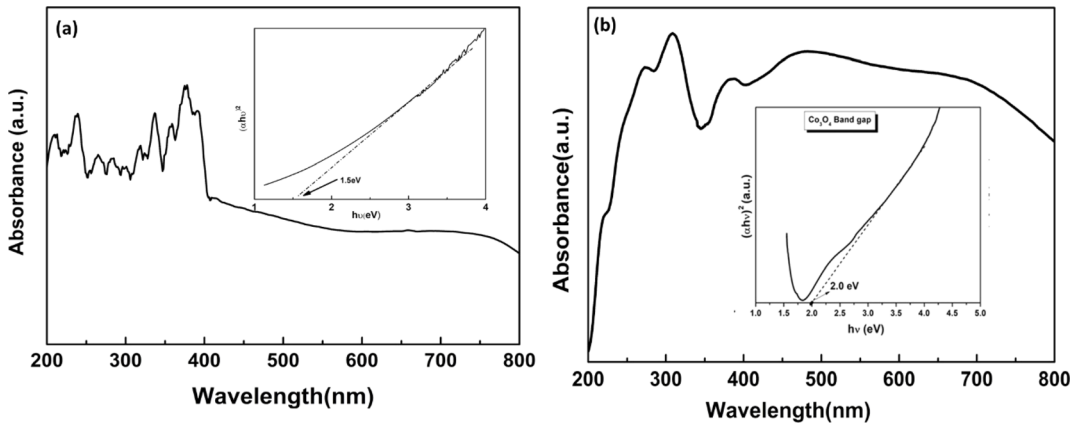

Fig. 4 UV-Vis DRS of CBG-10 and inset Tauc plot (a) and of Co_3O_4 (b).

Moreover, the UV-Vis Diffuse Reflectance Spectroscopy (DRS) analysis conducted on aged samples unveiled the absence of discernible absorption peaks, a phenomenon potentially attributable to energy gaps induced by quantum confinement effects. The observed stability of the Co–O bond within the Co_3O_4 NPs can be attributed to the polar-symmetrical structure, further reinforced by weak van der Waals interactions within the nanoscale particle regime, resulting in a slightly broader absorption peak.[23]

$$\alpha h\nu = A(h\nu - E_g)^n \quad (3)$$

The X-ray Photoelectron Spectroscopy (XPS) analysis was conducted to ascertain the elemental composition and chemical states within the CBG-10 composite as synthesized. Notably, the XPS survey spectrum (Fig. 5) underscores the exceptional purity of the synthesized material, revealing prominent peaks corresponding to C 1s, N 1s, Co, and O 1s without the presence of any other elements. Further examination of the Co 2p peaks in Fig. 5 indicates the presence of Co_3O_4/rGO/biochar (CBG-10) within the photocatalyst, as evidenced by peaks observed at 781.4 eV and 797.1 eV, corresponding to Co $2p_{3/2}$ and Co $2p_{1/2}$, respectively. The presence of Co $2p_{3/2}$ peaks at 781.4 eV suggests the existence of Co^{2+} ions at tetrahedral sites, while additional peaks at 785.7 eV and 806.09 eV, classified as satellite peaks, indicate the prevalence of high-spin Co^{2+} ions at octahedral sites. Moreover, the O 1s peak in the survey spectrum confirms the presence of the oxide form within the composite. Additionally, the appearance of peaks at 284.8 eV in the C 1s spectrum suggests the coupling of sp^2 C atoms with N atoms in the biochar structure. These comprehensive XPS findings unequivocally demonstrate the coexistence of rGO, biochar, and Co_3O_4 within the CBG-10 composite, culminating in the formation of a heterostructure with potential implications for advanced photocatalytic applications.

3.1 PZC (point of zero charge)

In this experimental investigation, the determination of the point of zero charge (PZC) of the synthesized hybrid adsorbent CBG-10 proved to be a pivotal aspect influencing the efficacy of dye removal processes. The salt addition method was employed to compute the PZC, revealing a value of 7.2 (Fig. 6). This finding elucidates the behaviour of the CBG-10 surface, indicating a negative charge predominance when the pH of the solution surpasses the PZC. Such a characteristic renders the adsorbent more adept at removing cationic dyes like MG and MB from dye mixtures. Conversely, at pH levels below the PZC, the surface exhibits a positive charge, rendering it more suitable for hexavalent chromium removal. The experimental results further underscore the influence of pH on dye and chromium removal efficiencies. At pH 3.0, the degradation percentages of MB, MG, and Cr(VI) were 20.1, 23.2, and 98.4 respectively, while at pH 10.5, these percentages improved significantly to 96, 93, and 15 respectively. Notably, at pH 7.5, intermediate degradation percentages were observed for MB, MG, and Cr(VI) at 65, 60, and 54 respectively. These findings shed light on the pH-dependent performance of the CBG-10 adsorbent and provide valuable insights for optimizing dye and chromium removal processes in environmental remediation applications.

3.2 Adsorption performance

Fig. 7(a)–(c) depicts the adsorption outcomes of the CBG-10 composite, respectively. CBG-10 composites have high adsorption capacity under light-shielding circumstances for MB, MG, and Cr(VI) solutions. Significantly different. Loading the catalyst results in occupied active sites on the CBG-10. Loading the catalyst can restrict delicate pore structures, leading to decreased adsorption capacity. The adsorptive percentage removal of dye was determined to be (40.07, 37.65, 33.22, and 31.86) at various concentrations of methylene blue (40 ppm, 60 ppm, 80 ppm, and 100 ppm). For malachite green dye, the adsorptive removal percentage was determined to be (40.5, 38.2, 33.62, and 30.47) for 40 mg L^{-1}, 60 mg L^{-1}, 80 mg L^{-1}, and 100 mg L^{-1} loaded dye. Furthermore, the elimination of chromium(VI) was determined to be 44.38, 40.81, 38.75, and 34.75 for (10 mg L^{-1}, 20 mg L^{-1}, 30 mg L^{-1}, and 50 mg L^{-1}). The adsorptive percentage removal of dyes/Cr(VI) was measured using the formula

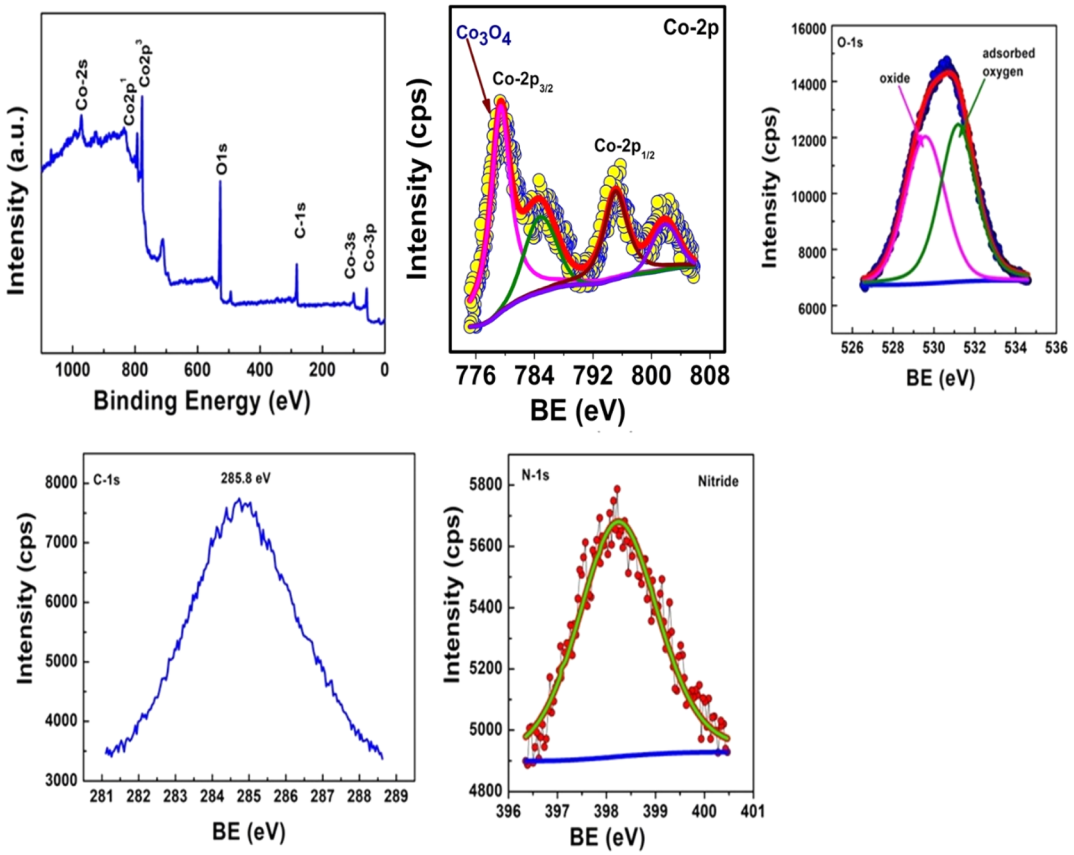

Fig. 5 XPS survey spectrum of 10CN–Co_3O_4, & high-resolution spectra for Co 2p, O 1s, C 1s and N 1s.

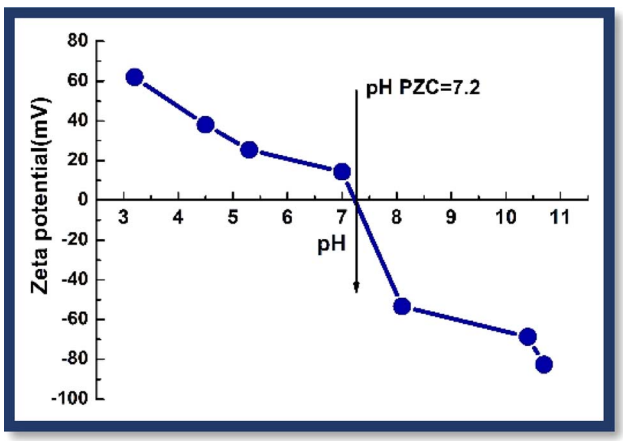

Fig. 6 PZC of an adsorbent CBG-10.

$$\text{Dye removal } (\%) = \frac{(C_0 - C_t)}{C_0} \times 100$$

4. Adsorption isotherm

The sorption isotherm, which is equally crucial in determining the right adsorption model, provides the maximum capacity of adsorption as well as the equilibrium connection between the sorbent and the sorbate.[26] Numerous isotherm models are available for both the interpretation of experimental data and for elucidating the equilibrium of adsorption. The equations for the Freundlich and Langmuir isotherms have been assessed in this study.

The homogenous adsorption of the dye molecule is the foundation of the Langmuir isotherm model, which depicts the behaviour of monolayer coverage in the absence of an interface between the adsorbate molecules. Once the dye molecules have completely covered the adsorbent site, it is assumed that no further adsorption occurs there.[26]

The Langmuir equation can be expressed as follows:

$$\frac{C_e}{q_e} = \frac{1}{K_L} + \frac{a_L}{K_L C_e} \quad (4)$$

where C_e and q_e (mg g^{-1}) stand for, respectively, the dye's residual concentration and its equilibrium amount of adsorbed dye. The Langmuir constants, a_L (L mg^{-1}), and the maximal Langmuir uptake capacity, K_L (L g^{-1}), are respectively.

The heterogeneous sorption on the surface with the interaction between adsorbate molecules is the foundation of the Freundlich adsorption isotherm. Multilayer adsorption results from the non-uniform energy distribution on the surface of this non-homogeneous system.[26] The model's linear form can be expressed as follows:

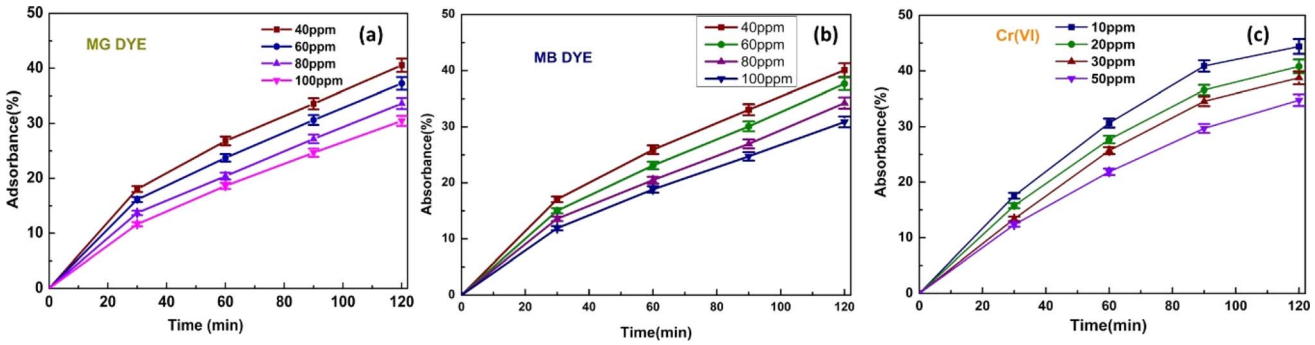

Fig. 7 (a)–(c) Adsorption of dyes/Cr(VI).

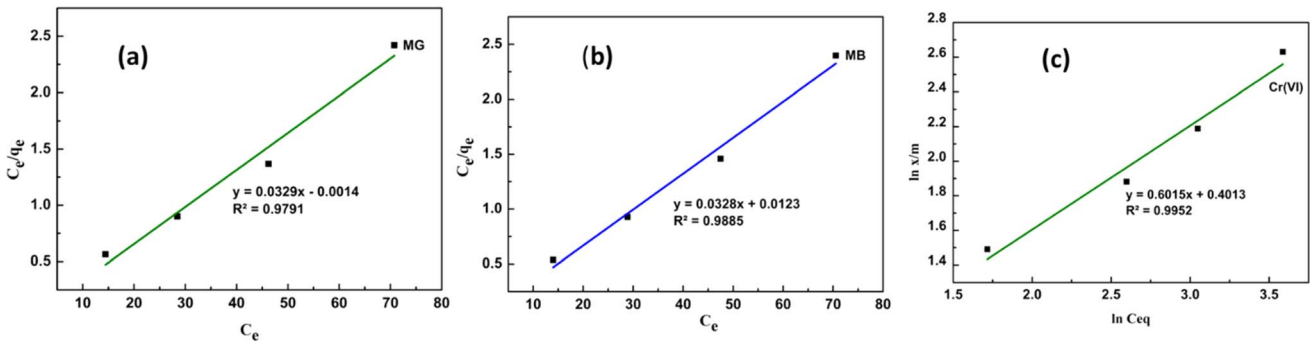

Fig. 8 Linear plots of Langmuir isotherm of MG (a) and MB (b) and Freundlich isotherm model of Cr(VI) respectively.

$$\log q_e = \log K_F + \frac{1}{n}\log C_e \quad (5)$$

where K_F and n are the Freundlich constants for the bonding energy and adsorption intensity, respectively.

The equilibrium isotherm for the adsorption of dyes (MB and MG) on the adsorbent molecule was established. From the experimental data, the Langmuir adsorption isotherm fitted well for CBG-10 (MB and MG) dyes in comparison to the other isotherm. The Freundlich adsorption well fitted for Cr(VI). The graphical representation of both isotherms was given in the Fig. 8(a) and (b) for MG and MB dyes.

4.1 Adsorption kinetics

Adsorption kinetics facilitates a relationship between the pseudo-first order, pseudo-second order, and intra-particle diffusion model, providing extensive information on the sorption process's steps and the maximum intake capacity of adsorbents. The linear form of all the above said kinetics models are given as follows:

$$\ln(q_e - q_t) = \ln q_e - K_1 t \quad (6)$$

$$\frac{t}{q_t} = \frac{1}{K_2 q_e^2} + \frac{1}{q_e t} \quad (7)$$

$$q_t = K_i t^{1/2} + C \quad (8)$$

where the rate constants for the above mentioned kinetics parameter for the adsorption process, respectively, are denoted by K_1 (min), K_2 (g mg^{-1} min^{-1}), and K_i (mg g min$^{-1/2}$). The amounts of dye adsorbed per unit mass of CBG-10 are q_e and q_t (mg g^{-1}), respectively, at equilibrium and time t. C (mg g^{-1}) is the boundary thickness constant at time t. It is evident that the pseudo-first-order kinetic model's R^2 value for the MG dye case Fig. 9(a)–(c) was well fitted. Additionally, a large discrepancy in residual sorption capacity (q_e) was discovered between computation and experiment, indicating a subpar pseudo-second-order fit to the results of the experiment. Pseudo-first-order kinetics data showed that the model linearly fits with incredibly high correlation coefficients ($R^2 > 0.99$) for all starting MG, MB dye concentrations and Cr(VI). The calculated q_e values in the case of pseudo-first-order kinetics also closely reflect MG/MB and Cr(VI), the real results that show the adsorption rates follow pseudo-second-order kinetics. The rate constants fluctuated significantly and the estimated q_e values rose as the initial dye concentration increased, indicating that chemisorption—the sharing and exchanging of electrons between the sorbent and the substrate—could be a possible limiting step. The values of the rate constant k decrease as the initial dye concentration increases because there is less competition for sorption surface sites at lower concentrations. Higher concentrations result in lower sorption rates because there is more competition for surface-active sites.

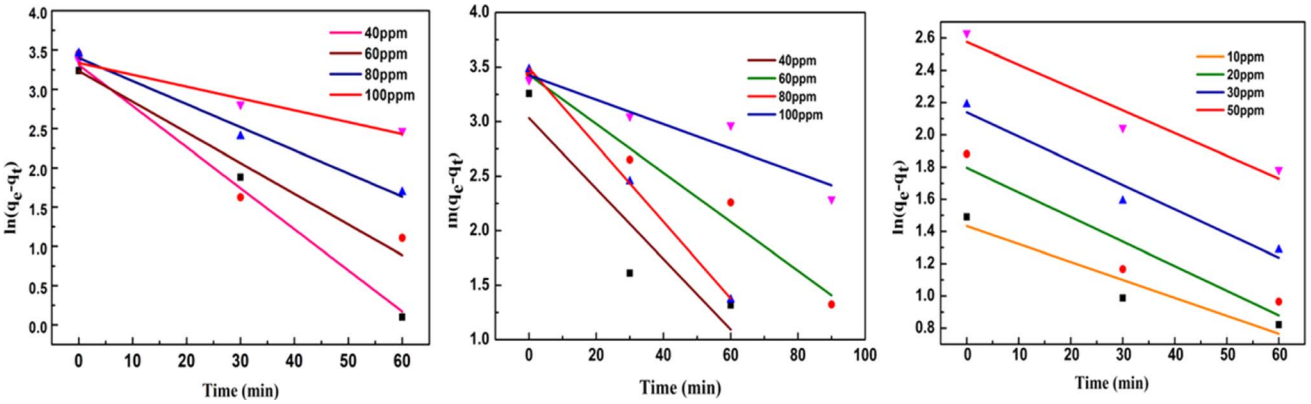

Fig. 9 Linear plots of pseudo-first-order kinetic models respectively at different initial MG, MB and Cr(VI) concentrations.

5. Test for photocatalytic activity

Fig. 10 illustrates the photoactive degradation of methylene blue (MB)/malachite green (MG) dyes and the heavy metal chromium(VI) dye under visible light irradiation over a period of 120 minutes, employing the CBG-*X* catalyst. Utilizing a simple photoreactor setup, the photocatalytic reactions were conducted by suspending 0.1 g of the catalyst in 150 mL of a 20 mg L^{-1} dye aqueous solution. The results presented in Fig. 11(a) and (b) reveal that the percentage of degradation achieved with the (rGO and biochar) catalyst at 10 weight percent reaches up to 100% under light illumination,

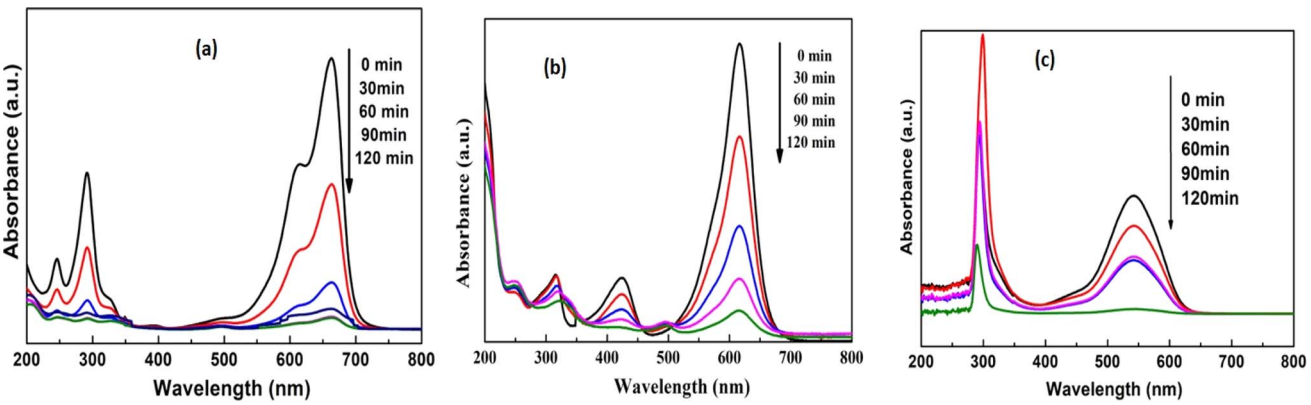

Fig. 10 UV-Vis spectrum analysis of MB (a), MG (b) and Cr(VI) (c).

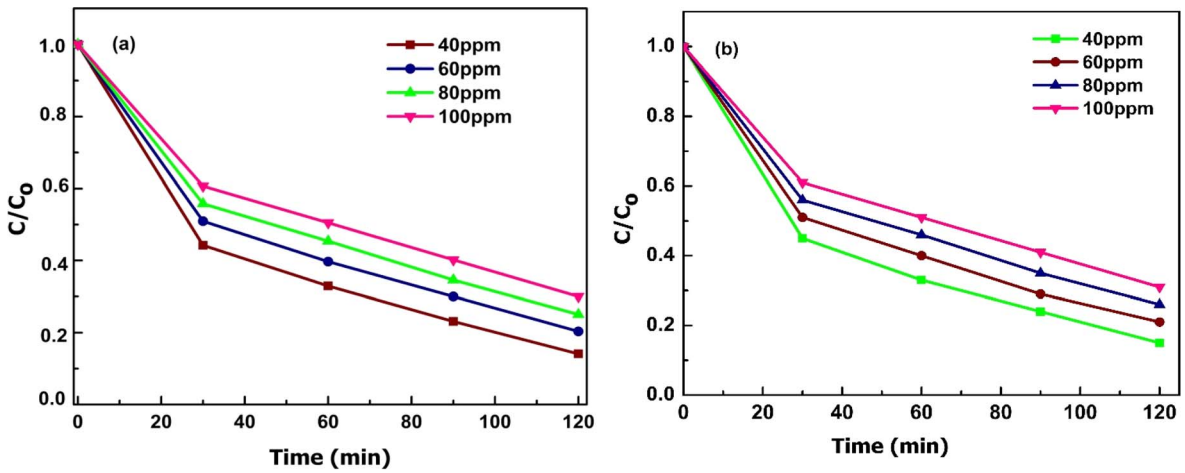

Fig. 11 Effect of illumination time of photodegradation of MG (a) and MB (b) at different initial concentrations by CBG-10.

Table 1 Comparison of efficiencies of various photocatalysts for degradation of MG and MB dyes with current work

Absorbent	Dye	% Dye degradation	Time (min)	References
10% Fe_2O_3/ZnO	MB	74	120 min	27
Oleic acid-modified cobalt oxide	Malachite green	66.6	100 min	28
ZnO	RhB	69	60 min	29
CBG10	MB, MG	98, 96	120 min	

surpassing the performance of individual catalyst components. Fig. 10(a)–(c) demonstrates the degradation kinetics of chromium(VI) and the MB/MG dye over the course of 0 to 120 minutes using CBG-10, while Fig. 11(b) depicts the gradual reduction in absorbance intensity corresponding to the total degradation of the dye with increasing illumination duration. Investigating the underlying mechanisms of photocatalytic degradation reveals the pivotal role of active oxidants and reductants, particularly hydroxyl radicals, superoxide radicals, and holes, as illustrated in Fig. 14. The combined action of electrons and superoxide radicals emerges as primary drivers of dye/Cr(VI) degradation, with holes contributing to a lesser extent. This understanding elucidates the fundamental mechanisms dictating the efficiency of photocatalytic contaminant removal, providing valuable insights for further research and development in this field (Table 1).

5.1 Various parameters affecting the photocatalytic degradation of dyes/Cr(VI)

5.1.1 Influence of contact time. Preliminary observations on dye (MG and MB) and Cr(VI) degradation Fig. 12(a)–(c) revealed that regardless of dye/Cr(VI) concentration, there is an initial rapid progression of dye/Cr(VI) degradation followed by a relatively slower adsorption until a plateau is reached, owing to a decrease in the number of active adsorption sites accessible for adsorption with time. As seen in the figure above, the dynamic equilibrium between dye adsorption and desorption was established within 30 minutes, and all subsequent degradation tests were conducted with the degradation time fixed at 2 hours.

5.1.2 Influence of pH. The pH of the solution is a major contributing factor to overall degradation of dyes and Cr(VI) on the catalyst. It influences the surface charges of catalyst and

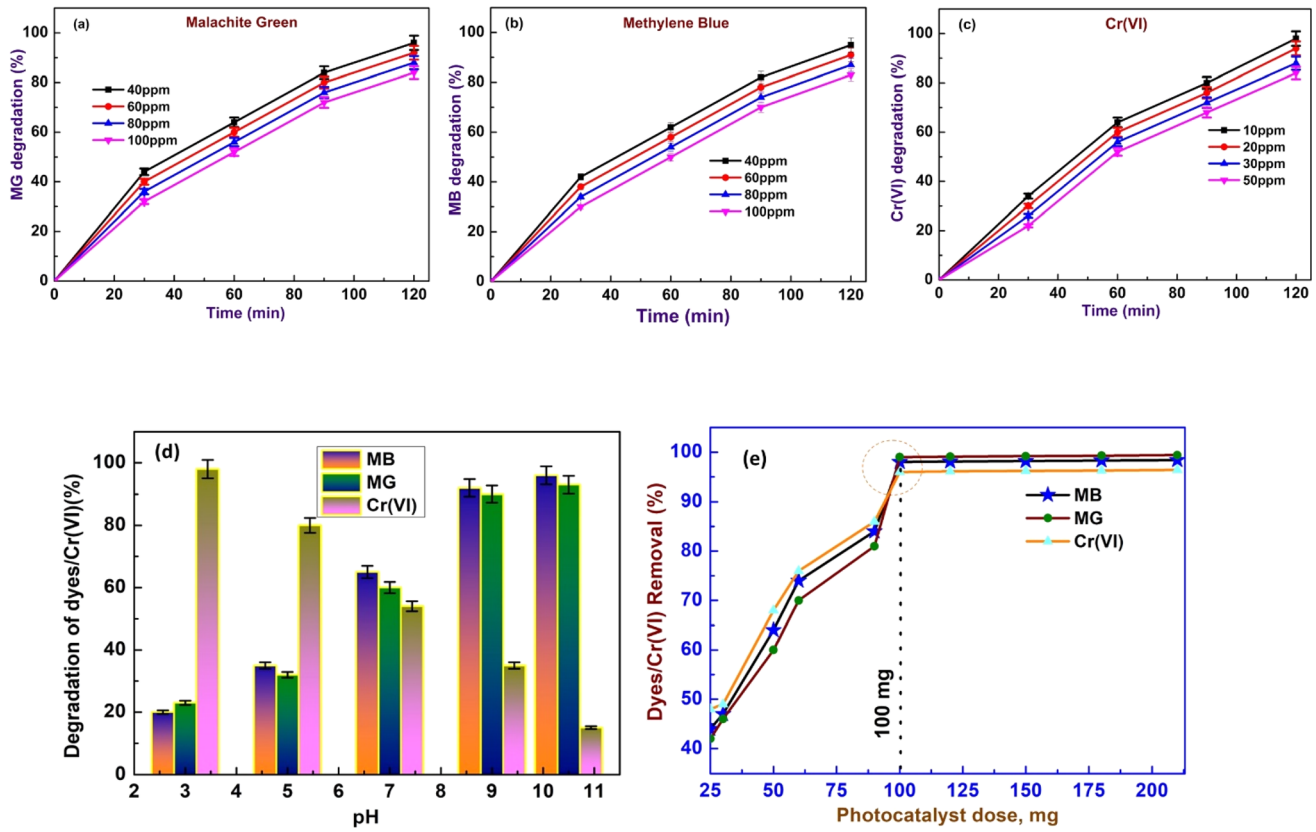

Fig. 12 (a)–(c) Effect of contact time on degradation of dyes/Cr(VI). (d) Influence of pH and (e) influence of photocatalyst dose on degradation of dyes/Cr(VI).

alters the degree of ionization/species of both adsorbent and adsorbate. To ascertain the effect of pH, adsorption of dyes/Cr(VI) were carried out within the pH range 3 to 10.4 and the results obtained are presented in Fig. 6.

As shown in Fig. 6 and 12(d) the PZC has a progressive decrease in Cr(VI) degradation with increasing pH, but the cationic dyes MB and MG have an increase in degradation with increasing pH. Like Cr(VI), the degradation of Cr(VI) is found to decrease with increasing pH, as is observed in the majority of catalysts. The increased amount of Cr(VI) degradation at acidic pH might be explained by stronger electrostatic contacts between negatively charged Cr(VI) molecules and protonated CBG-10 surface, which decreased at higher pH due to the creation of surface negative charge on CBG-10. In the case of MB and MG, which exist as cationic species above pH 4.0, the creation of surface negative charge on CBG-10 at higher pH allows for stronger electrostatic contact with MB and MG molecules, resulting in increased MB and MG breakdown. In the acidic pH range (pH 2 to 6.5), $HCrO_4^-$ is the dominating species, which gradually converts to CrO_4^{2-} as pH increases. Obviously, better electrostatic interaction between positively charged CBG-10 and negatively charged Cr(VI) species is expected at acidic pH, but reduces dramatically at higher pH due to deprotonation of CBG-10. Furthermore, the presence of extra OH at alkaline pH may compete with anionic Cr(VI) species to reduce degradation.

5.1.3 Influence of photocatalyst dose. In the investigation of the impact of CBG-10 dose on the removal efficiency of MG, MB, and Cr(VI) dyes, a systematic exploration was undertaken by varying the concentration of CBG-10 from 25 to 200 mg under standardized conditions of pH 7, room temperature, and 20 ppm initial concentrations of MG, MB, and Cr(VI). The results, as illustrated in Fig. 12(e), unequivocally demonstrate a discernible correlation between CBG-10 dosage and dye elimination percentage. At lower concentrations of CBG-10, a subdued dye-adsorption percentage was observed, attributed to an insufficient availability of active surface sites. However, as the CBG-10 dose was augmented, a significant enhancement in dye removal percentage was observed, reaching peak efficiencies at 100 mg of CBG-10 (>99%, 98% and 96% for MG, MB, and Cr(VI)). This optimal CBG-10 concentration showcased a saturation effect, indicating that further escalation of CBG-10 amounts would be redundant, as the elimination percentage exhibited minimal variations. Consequently, it is deduced that 100 mg of CBG-10 proves to be adequately efficacious for the simultaneous removal of MG, MB, and Cr(VI), providing valuable insights for future applications in water treatment processes.

5.1.4 Photocatalytic reduction of Cr(VI) into Cr(III). In the presence of CBG-10, the $Cr_2O_7^{2-}$ absorption band moves from 257.08 nm to 347 nm. This new elevated peak fades and disappears after 2 hours. As previously stated, the colour of the solution shifts from deep yellow to colourless, indicating that

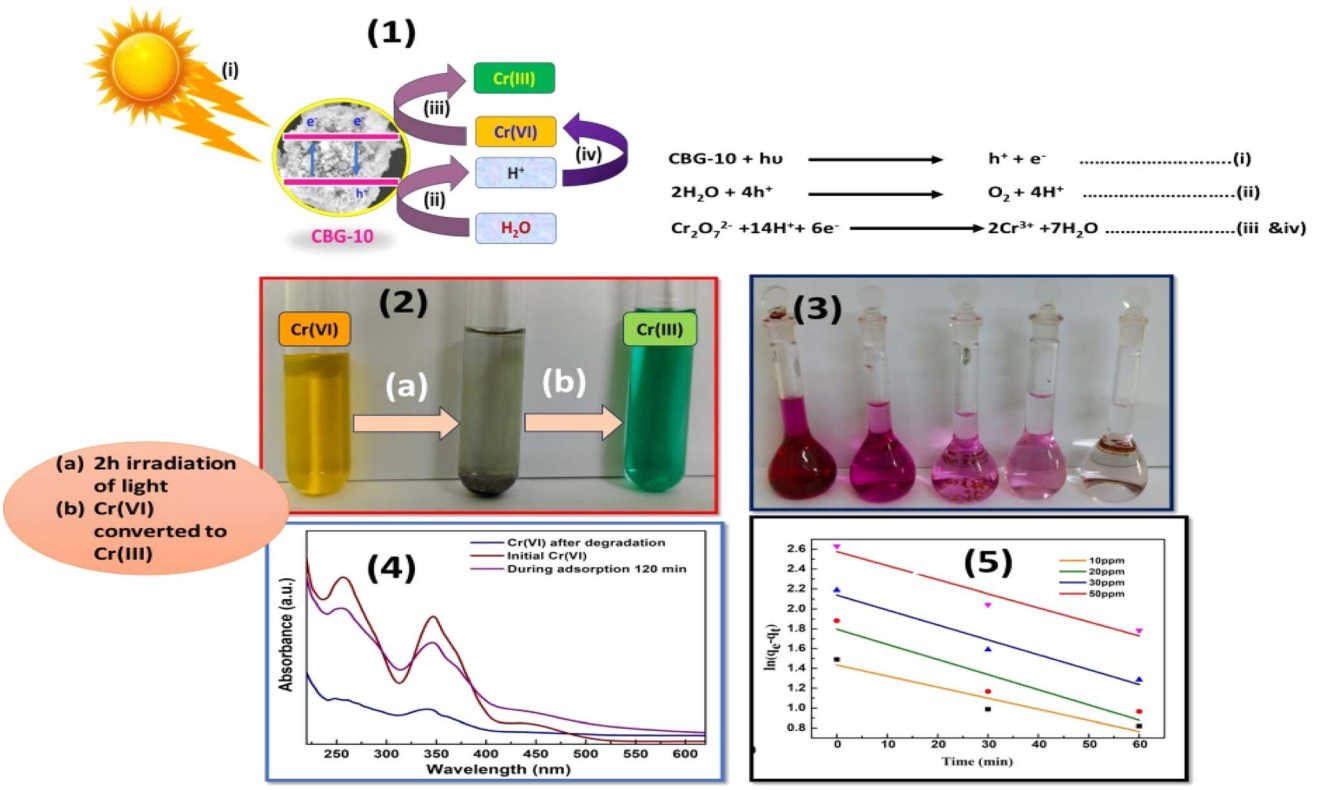

Fig. 13 (1) Schematic representation of plausible reaction mechanism of photocatalytic reduction of Cr(VI) to Cr(III) under the illumination of light by CBG-10; (2)–(4) photo reduction of Cr(VI)to Cr(III) and (5) pseudo first order linear fit with varying concentration.

Cr(VI) has been completely converted to less toxic Cr(III) by CBG-10 as shown in Fig. 13(4).

CBG-10 was utilized to photocatalyzed the reduction of Cr(VI) to Cr(III) in synthetic polluted water using potassium dichromate and using photocatalytic reactor. The current study suggests that photocatalysts can reduce Cr(VI) concentrations ranging from 10 ppm to 50 ppm to Cr(III) with the same dose. Fig. 13(1)–(5) shows how CBG-10 affects photocatalysis. To achieve adsorption–desorption equilibrium, the Cr(VI) was stirred continuously for 30 minutes in absence of light then light was illuminated Fig. 13(1)–(5). The photo-reduced solutions were then collected every 15 minutes for UV-Vis measurement. The residual Cr(VI) concentrations after photoreduction were measured using a UV-Vis spectrophotometer at 540 nm and the diphenylcarbazide (DPC) assays shown in Fig. 13(3).[30] The initial concentration of Cr(VI), expressed as C/Co, decreases continuously over time. The photocatalytic reduction of Cr(VI) by CBG-10 exhibits pseudo first-order kinetics with a high R^2 value (Fig. 13(5)). Fig. 13(1) shows a possible process for photocatalytic Cr(VI) reduction using CBG-10. Light irradiation causes the formation of holes and electrons in the valence and conduction bands of CBG-10 (see eqn (i)). Photo-induced holes react with water molecules, producing highly reactive h^+ (see eqn (ii)). Eqn (iii) shows that photo-induced electrons initially react with Cr(VI) near the CBG-10 edge. Eqn (iv) illustrates how highly reactive protons and electrons convert Cr(VI) to Cr(III). The schematic mechanism explains why harmful Cr(VI) can be reduced to less toxic Cr(III) through photocatalysis. However, increasing the pH towards the basic side reduces the photoreduction effectiveness of CBG-10. Therefore, an acidic pH is necessary. After adding NaOH solution, Cr(III) precipitates as hydroxides and separates from water.[31]

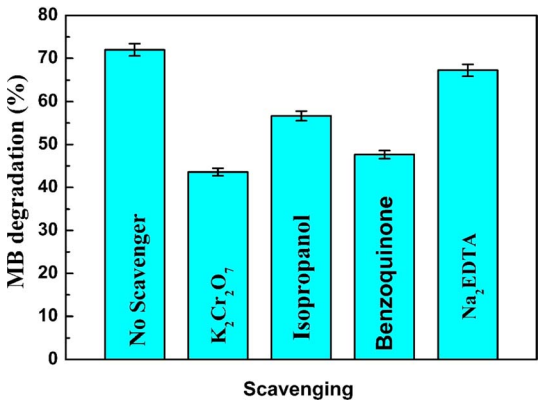

Fig. 14 Scavengers trapping experiments for photodegradation of MB over CBG-10 catalyst.

6. Scavenging study

To elucidate the involvement of reactive oxidants and reductants in the photocatalytic degradation process, a series of experiments employing various quenchers was conducted. Specifically, 1 mm benzoquinone was used to trap superoxide radicals ($^{-}\cdot O_2$), 20 mL of isopropanol for trapping hydroxyl radicals ($^{\cdot}OH$), and 1 mm of disodium EDTA for trapping holes (h^+).[25] The reduction in photodegradation efficiency upon the addition of these quenchers indicates the participation of superoxide radicals and holes in the degradation of malachite green (MG) and methylene blue (MB). In a scavenger trapping experiment involving high-concentration MB (80 mg L^{-1}) in the presence of the CBG-10 composite, the addition of disodium EDTA led to a 4% decrease in photodegradation percentage, suggesting a lesser role of holes in the degradation process. Furthermore, a significant decrease in degradation percentage was observed when benzoquinone, isopropanol, and potassium dichromate were used as scavengers, indicating the reduction of superoxide radicals, hydroxyl radicals, and electrons on the catalyst surface. From these findings, it can be inferred that superoxide radicals, hydroxyl radicals, and electrons primarily contribute to the degradation process facilitated by this catalyst. As given in Fig. 14.

7. Reusability study

Examining the method' affordability and applicability was done by looking at CBG-10's stability and reusability. During the degradation process, the CBG-10 hybrid composite was detached using 0.5 M of acetone from the solution. The hybrid composite was then cleaned with distilled water and reused for the degradation of new MG and MB dye solution. The study's findings are presented in Fig. 15. The photocatalyst

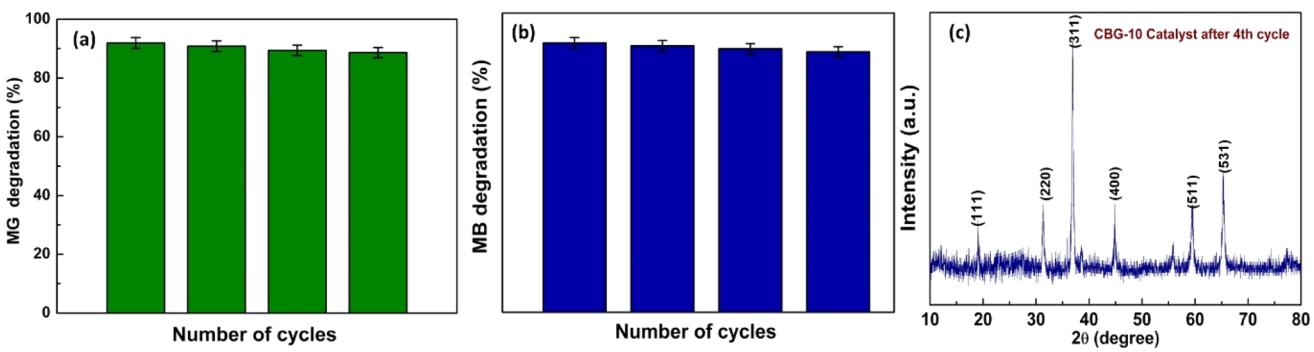

Fig. 15 Recyclability of the (c) catalyst CBG-10 for the photodegradation of (a) malachite green and (b) methylene blue respectively.

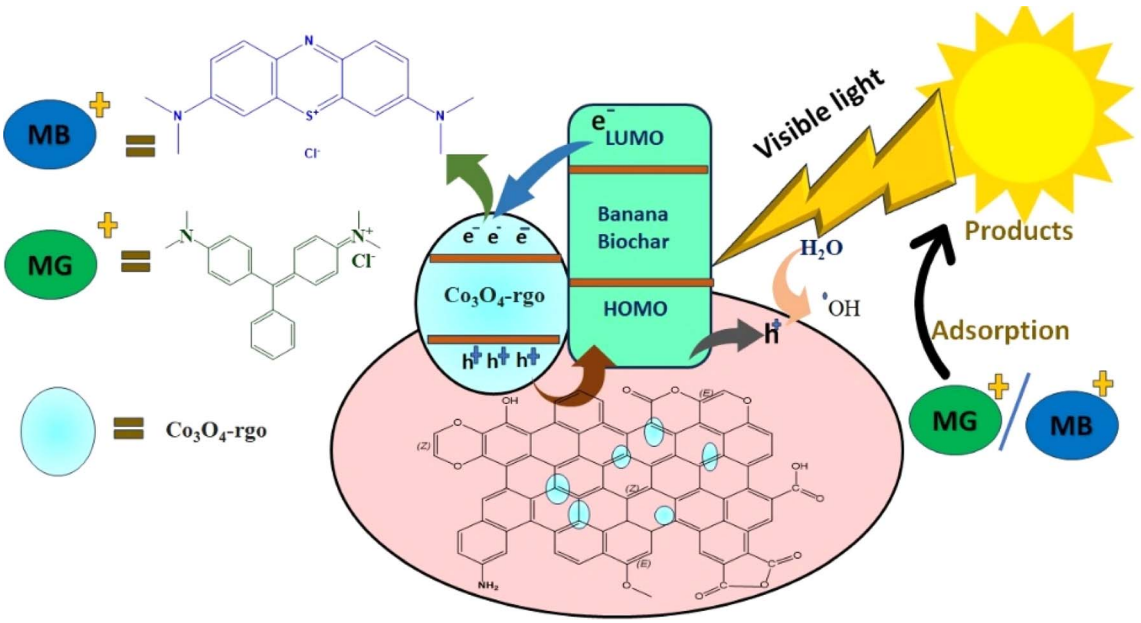

Fig. 16 Plausible mechanism of photodegradation of dye using CBG-10.

performance shows no discernible change after four cycles of visible light exposure, proving that the CBG-10 hybrid composite is a reliable and effective photocatalyst for the breakdown of MG and MB dye.

8. Photocatalysis mechanism

The investigation into the quenching reaction, conducted by introducing specific quenchers, aims to elucidate the reactive species involved in the degradation of pollutants by the Co_3O_4/rGO and biochar catalyst. This analysis is crucial for understanding the underlying mechanism driving pollutant degradation. The observed significantly elevated photocatalytic activity in the CBG-10 composite underscores the importance of the interaction and synergistic effects between Co_3O_4/rGO and biochar. The successful induction of electron–hole pair separation within this coupling system highlights its effectiveness in promoting photocatalytic activity.

Schematically depicted in Fig. 16, the photodegradation process of the rGO/Co_3O_4 and biochar hybrid composite under visible light involves intricate mechanisms. Upon exposure to visible light, electrons are excited from the biochar's valence band to its conduction band, generating electron–hole pairs. To mitigate charge carrier recombination, electrons migrate from the biochar's conduction band to the conduction band of rGO/Co_3O_4. Concurrently, positively charged holes are formed on the valence band of rGO/Co_3O_4 and injected into the highest occupied molecular orbital (HOMO) of biochar. This orchestrated electron–hole pair separation, facilitated by the coupling system, establishes a type-II heterojunction configuration, thereby preventing recombination and enhancing photocatalytic activity.

The ternary composite's superior dye degradation activity, coupled with its demonstrated stability, suggests its potential applicability in real-world scenarios for the cleanup of dyes and other contaminants. This heightened performance, surpassing that of both binary and ternary systems, underscores the efficacy of the Co_3O_4/rGO and biochar composite in pollutant remediation applications. Further research into optimizing the composition and structure of such ternary composites could lead to enhanced efficiency and broader applicability in environmental remediation efforts.

9. Conclusion

The present study underscores the promising potential of CBG-10 as a highly efficient and environmentally benign photocatalyst for the removal of various pollutants, including MG, MB, and Cr(VI), under visible light irradiation. The development of a recyclable CBG-10 composite, exhibiting excellent properties and significant morphological interactions, further enhances its applicability and sustainability. Our investigation into the recyclability of CBG-10 revealed a negligible decrease (<5%) in degradation efficiency after four successive cycles, indicative of its remarkable stability and sustained activity. Comparative analysis against other binary and ternary systems highlights the superior performance and stability of the CBG-10 composite, emphasizing its suitability for practical applications in pollutant remediation. While this study lays a strong foundation for understanding the efficacy of CBG-10 in laboratory settings, further exploration is warranted to assess its performance in treating actual wastewater. Such endeavours would validate its practical utility and promote its adoption in real-world scenarios. Looking ahead, the optimized catalyst combination demonstrated in this research holds promise for broader applications beyond pollutant removal, including water splitting and CO_2 reduction. Continued research efforts in this direction can unlock

the full potential of CBG-10 and pave the way for sustainable solutions to environmental challenges.

Author contributions

Amrita Priyadarsini: investigation, writing – original draft, visualization, conceptualization. Chirasmayee Mohanty: editing – original draft, formal analysis, methodology, visualization. Spandan Nanda: software, formal analysis, conceptualization, editing original draft. Abinash Mishra: data curation, formal analysis, editing original draft. Nigamananda Das: methodology, supervision. Nandita Swain: supervision. Manasi Dash: supervision, visualization, software. Pradip Kumar Jena: supervision.

Conflicts of interest

There are no conflicts to declare.

Acknowledgements

Amrita Priyadarsini is very grateful to the CIF, OUAT university for the support. This work constitutes the Ph.D. work of the first author. This work was supported by Department of Chemistry, Utkal University, Odisha.

References

1 C. Han, L. Ge, C. Chen, Y. Li, X. Xiao, Y. Zhang and L. Guo, Novel visible light induced Co_3O_4-g-C_3N_4 heterojunction photocatalysts for efficient degradation of methyl orange, *Appl. Catal., B*, 2014, **147**, 546–553.

2 Y. Luo, J. Luo, W. Zhou, X. Qi, H. Zhang, Y. W. Denis, T. Yu, *et al.*). Controlled synthesis of hierarchical graphene-wrapped TiO_2@Co_3O_4 coaxial nanobelt arrays for high-performance lithium storage, *J. Mater. Chem. A*, 2013, **1**(2), 273–281.

3 M. Bhagat, R. Anand, R. Datt, V. Gupta and S. Arya, Green synthesis of silver nanoparticles using aqueous extract of Rosa brunonii Lindl and their morphological, biological and photocatalytic characterizations, *J. Inorg. Organomet. Polym. Mater.*, 2019, **29**, 1039–1047.

4 A. Singh, A. Ahmed, A. Sharma, C. Sharma, S. Paul, A. Khosla, S. Arya, *et al.*). Promising photocatalytic degradation of methyl orange dye via sol-gel synthesized Ag–CdS@Pr-TiO_2 core/shell nanoparticles, *Phys. B*, 2021, **616**, 413121.

5 B. Singh, A. Singh, A. Sharma, P. Mahajan, S. Verma, B. Padha, S. Arya, *et al.*). Electrochemical sensing and photocatalytic degradation of 2,4-dinitrophenol via bismuth(III) oxide nanowires, *J. Mol. Struct.*, 2022, **1255**, 132379.

6 A. Sharma, A. Singh, A. Khosla and S. Arya, Preparation of cotton fabric based non-invasive colorimetric sensor for instant detection of ketones, *J. Saudi Chem. Soc.*, 2021, **25**(10), 101340.

7 E. D. Lester, G. Aksomaityte, J. Li, S. Gomez, J. Gonzalez-Gonzalez and M. Poliakoff, Controlled continuous hydrothermal synthesis of cobalt oxide (Co_3O_4) nanoparticles, *Prog. Cryst. Growth Charact. Mater.*, 2012, **58**(1), 3–13.

8 M. A. Laguna-Marco, D. Haskel, N. Souza-Neto, J. C. Lang, V. V. Krishnamurthy, S. Chikara, M. van Veenendaal, *et al.*). Orbital magnetism and spin-orbit effects in the electronic structure of $BaIrO_3$, *Phys. Rev. Lett.*, 2010, **105**(21), 216407.

9 L. B. Liao, Q. H. Zhang, Z. H. Su, Z. Z. Zhao, Y. N. Wang, Y. Li, X. X. Lu, D. G. Wei, G. Y. Feng, Q. K. Yu, X. J. Cai, J. M. Zhao, Z. F. Ren, H. Fang, F. Robles-Hernandez, S. Baldelli and J. M. Bao, Efficient solar water-splitting using a nanocrystalline CoO photocatalyst, *Nat. Nanotechnol.*, 2014, **9**, 69–73.

10 H. R. Pouretedal and M. Kiyani, Photodegradation of 2-nitrophenol catalyzed by CoO, CoS and CoO/CoS nanoparticles, *J. Iran. Chem. Soc.*, 2014, **11**, 271–277.

11 V. Skumryev, S. Stoyanov, Y. Zhang, G. Hadjipanayis, D. Givord and J. Nogués, Beating the superparamagnetic limit with exchange bias, *Nature*, 2003, **423**(6942), 850–853.

12 H. K. Lin, H. C. Chiu, H. C. Tsai, S. H. Chien and C. B. Wang, Synthesis, characterization and catalytic oxidation of carbon monoxide over cobalt oxide, *Catal. Lett.*, 2003, **88**, 169–174.

13 K. Nakaoka, M. Nakayama and K. Ogura, Electrochemical deposition of spinel-type cobalt oxide from alkaline solution of Co^{2+} with glycine, *J. Electrochem. Soc.*, 2002, **149**(3), C159.

14 W. Peng, H. Li, Y. Liu and S. Song, A review on heavy metal ions adsorption from water by graphene oxide and its composites, *J. Mol. Liq.*, 2017, **230**, 496–504.

15 O. M. Bankole, S. E. Olaseni, M. A. Adeyemo and A. S. Ogunlaja, Microwave-assisted synthesis of cobalt oxide/reduced graphene oxide (Co_3O_4–rGo) composite and its sulfite enhanced photocatalytic degradation of organic dyes, *Zeitschrift für Physikalische Chemie*, 2020, **234**(10), 1681–1708.

16 S. Li, T. Zhu, L. Dong and M. Dong, Boosted visible light photodegradation activity of boron doped rGO/gC_3N_4 nanocomposites: the role of C–O–C bonds, *New J. Chem.*, 2018, **42**(21), 17644–17651.

17 R. Suresh, R. Udayabhaskar, C. Sandoval, E. Ramírez, R. V. Mangalaraja, H. D. Mansilla, J. Yáñez, *et al.*). Effect of reduced graphene oxide on the structural, optical, adsorption and photocatalytic properties of iron oxide nanoparticles, *New J. Chem.*, 2018, **42**(11), 8485–8493.

18 X. Li, R. Shen, S. Ma, X. Chen and J. Xie, Graphene-based heterojunction photocatalysts, *Appl. Surf. Sci.*, 2018, **430**, 53–107.

19 W. S. Hummers Jr and R. E. Offeman, Preparation of graphitic oxide, *J. Am. Chem. Soc.*, 1958, **80**(6), 1339.

20 P. B. Koli, K. H. Kapadnis, U. G. Deshpande and M. R. Patil, Fabrication and characterization of pure and modified Co_3O_4 nanocatalyst and their application for photocatalytic degradation of eosine blue dye: a comparative study, *J. Nanostruct. Chem.*, 2018, **8**, 453–463.

21 R. K. Gupta, A. K. Sinha, B. N. Raja Sekhar, A. K. Srivastava, G. Singh and S. K. Deb, Synthesis and characterization of

various phases of cobalt oxide nanoparticles using inorganic precursor, *Appl. Phys. A: Mater. Sci. Process.*, 2011, **103**, 13–19.

22 M. Salavati-Niasari, N. Mir and F. Davar, Synthesis and characterization of Co_3O_4 nanorods by thermal decomposition of cobalt oxalate, *J. Phys. Chem. Solids*, 2009, **70**(5), 847–852.

23 G. Chen, X. Si, J. Yu, H. Bai and X. Zhang, Doping nano-Co_3O_4 surface with bigger nanosized Ag and its photocatalytic properties for visible light photodegradation of organic dyes, *Appl. Surf. Sci.*, 2015, **330**, 191–199.

24 S. Jamil, H. Ahmad, S. R. Khan and M. R. S. A. Janjua, The first morphologically controlled synthesis of a nanocomposite of graphene oxide with cobalt tin oxide nanoparticles, *RSC Adv.*, 2018, **8**(64), 36647–36661.

25 X. Liu, G. Li, C. Chen, X. Zhang, K. Zhou and X. Long, Banana stem and leaf biochar as an effective adsorbent for cadmium and lead in aqueous solution, *Sci. Rep.*, 2022, **12**(1), 1584.

26 S. Vijayalakshmi, E. Elanthamilan, J. P. Merlin and I. S. Lydia, Tuning the efficiency of $CoFe_2O_4$@rGO composite by encapsulating Ag nanoparticles for the photocatalytic degradation of methyl violet dye and energy storage systems, *New J. Chem.*, 2021, **45**(37), 17642–17653.

27 M. Saeed, M. Siddique, M. Usman, A. ul Haq, S. G. Khan and H. A. Raoof, Synthesis and characterization of zinc oxide and evaluation of its catalytic activities for oxidative degradation of rhodamine B dye in aqueous medium, *Zeitschrift für Physikalische Chemie*, 2017, **231**(9), 1559–1572.

28 D. A. Ali, E. E. El-Katori and E. A. Kasim, Sol-gel sonochemical Triton X-100 templated synthesis of Fe_2O_3/ZnO nanocomposites toward developing photocatalytic degradation of organic pollutants, *Zeitschrift für Physikalische Chemie*, 2021, **235**(3), 239–263.

29 M. Verma, M. Mitan, H. Kim and D. Vaya, Efficient photocatalytic degradation of malachite green dye using facilely synthesized cobalt oxide nanomaterials using citric acid and oleic acid, *J. Phys. Chem. Solids*, 2021, **155**, 110125.

30 N. K. Verma, P. Khare and N. Verma, Synthesis of iron-doped resorcinol formaldehyde-based aerogels for the removal of Cr(VI) from water, *Green Process. Synth.*, 2015, **4**(1), 37–46.

31 Y. Zhong, X. Qiu, D. Chen, N. Li, Q. Xu, H. Li, J. Lu, *et al.*). Flexible electrospun carbon nanofiber/tin(IV) sulfide core/sheath membranes for photocatalytically treating chromium(VI)-containing wastewater, *ACS Appl. Mater. Interfaces*, 2016, **8**(42), 28671–28677.